POLITECNICO DI TORINO
Repository ISTITUZIONALE

Artificial Intelligence Driven Earthquakes Early Detection in Noisy Urban Areas

(Article begins on next page)

07 March 2025

Artificial Intelligence Driven Earthquakes Early Detection in Noisy Urban Areas

Hasan Awad[1*], Fehmida Usmani[1,2], Emanuele Virgillito[1], Rudi Bratovich[3], Stefano Straullu[4],
Francesco Aquilino[4], Roberto Proietti[1], Rosanna Pastorelli[3] and Vittorio Curri[1]

1. Department of Electronics and Telecommunications, Politecnico di Torino, Turin, Italy
2. National University of Sciences & Technology (NUST), Islamabad, Pakistan
3. SM-Optics, 20093, Cologno Monzese, Italy
4. LINKS Foundation, 10129, Turin, Italy

hasan.awad@polito.it

Abstract—In this study, we introduce a novel approach for early earthquake detection in urban environments with high ambient noise. By using machine learning techniques to analyze the polarization alterations of light traveling along an existing traffic-carrying optical network, we demonstrate a cost-effective, secure, and efficient solution for detecting primary earthquake wave in noisy conditions. Detecting the primary wave preceding a destructive surface earthquake wave enables the rapid initiation of emergency plans, ensuring timely implementation of earthquake countermeasures. Our methodology involves collecting large dataset of polarization angular speed evolution along a fiber cable to conduct a Monte Carlo analysis, after integrating the strains induced by car passages over those induced by real earthquake ground displacement values. This dataset trains a machine learning model that leverages a deep learning architecture based on Long Short - Term Memory layers and attention mechanism. The model's training and validation show high accuracy rates, implying that additional training is unlikely to yield significant improvements, resulting in a 99% correct detection rate for multi-class classification of all events. The model demonstrates high accuracy in distinguishing between various environmental events, providing accurate early warning signals upon primary wave detection.

Index Terms—earthquakes, polarization, machine-learning, early-warnings, optical-networks, sensing, waveplate-model, ambient-noise

I. INTRODUCTION

The global Distributed Fiber Optic Sensor (DFOS) market size was valued at USD 1.60 billion in 2023 and expected to grow at a Compound Annual Growth Rate of 6.5% from 2024 to 2030. DFOS is driving increased investments and development efforts by enterprises world-wide due to their broad applications across various industries, including Energy, Oil & Gas, Civil, Aerospace, Seismology and others, enabling real-time data-driven monitoring [1] [2]. These sensing techniques can measure slow-varying environmental variables influenced by external events, at any point along the fiber's length with high spatial resolution. DFOS generally operates based on the linear and non-linear back-scattering phenomena within an optical fiber such as Rayleigh scattering and Raman/Brillouin scattering, respectively [3] [4]. Unlike Brillouin and Rayleigh

scattering, Raman scattering is only temperature dependent, which enables Distributed Temperature Sensing (DTS) that has been successfully employed in several scenarios such as detecting pipeline leaks [5]. Rayleigh scattering, when combined with Optical Time Domain Reflectometry (OTDR) or Optical Frequency Domain Reflectometry (OFDR) has allowed the development of Distributed Acoustic Sensing (DAS). DAS utilizes an optoelectronic interrogator to transmit short light pulses into the fiber cable and then measures the optical perturbations in the back-scattered light, thereby deriving strain-rate signals that are proportional to the amount of external stress impacting the fiber [6]. Recently we have witnessed an increasing interest in DAS within the field of Geophysics, particularly in Seismology and earthquake early detection [7]. In [8], the authors show that a submarine fiber optic DAS system can reduce alert time by 3 seconds compared to land-based stations. However, DAS systems require dedicated dark fibers, limiting the overall data-carrying capacity. These systems are also incompatible with inline optical amplifiers because the optical isolators inside the amplifiers block the back-scattered DAS signal. Although these amplifications could be removed along dark fibers, however, this would lead to significant signal attenuation. Furthermore, the usable range of DAS systems is less than 100 km [6]. Interferometric techniques came to overcome the issue of DAS usable range. These techniques can measure femto-seconds delay experienced by the light propagating along the fiber at a micrometer scale and over several thousands of kilometers [9]. But still, Interferometric techniques require dedicated and expensive ultra-stable low-phase lasers. Unlike DAS and Interferometric techniques, State-of-Polarization (SOP) sensing approach requires no dedicated fibers or expensive equipment, but rather exploits the extensively deployed traffic-carrying optical network with no data security issues [10] [11] [12], and by utilizing a simple Polarimeter or a simpler Polarization Beam Splitter as a polarization sensing device [13]. This approach is empowered by Machine Learning (ML) to analyze the integrated polarization alterations, induced by external events, in the modulated light traveling along the fiber. In [14] and [15], we leveraged this approach for anthropic activity sensing, particularly for car passage/traffic, using Intensity

Modulated-Direct Detected (IM-DD) optical signals in terrestrial telecommunication networks, exploiting a single sensing fiber cable. The experiment showed capability to detect and localize events with an accuracy of less than 100 meters. While in [16], we examine the same approach, utilizing two sensing fibers for early earthquake detection by identifying the pattern of SOP changes induced by a primary earthquake wave. A Primary wave usually precedes an earthquake's destructive surface wave by tens of seconds, allowing for early warning generation and swift initiations for emergency response. We extend the scope of the work in [10] to exploit the use of interconnected optical mesh network across three different municipalities as a unified sensing and epicenter localization grid. By utilizing real ground displacement data from seven earthquakes of magnitudes ranging from 4 to 6, along with a Waveplate simulator, we collected large dataset of SOP evolution to train an ML model. Upon testing the model, we achieve 98% accuracy in detecting primary wave arrival. This system provides a time lag of 21 seconds for nearby municipalities and 57 seconds for more distant areas before the arrival of destructive surface wave, surpassing the early warning time of DAS and covering larger areas than interferometric techniques, without the need for additional dedicated or expensive equipment. Our previous studies assume no other events occurring simultaneously with the earthquake, which does not reflect actual scenarios where multiple factors can influence the polarization of light along the fiber such as civil works, car passage, heavy machinery operations and others.
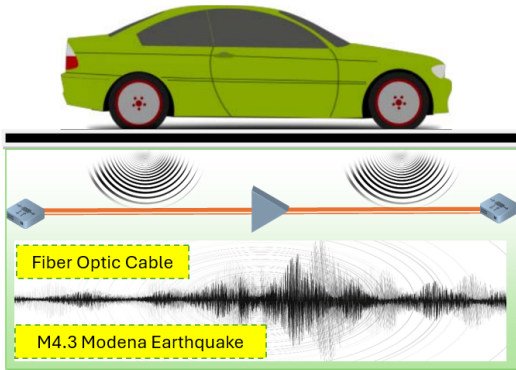

Fig. 1. Real-World Noisy Environment - The fiber cable is stressed by an earthquake occurring simultaneously with an environmental event

Therefore, to mimic real world-conditions as shown in Fig. 1, this manuscript will consider incorporating the strain induced by a car passage recorded by DAS over strain induced by real ground displacement data from an M4.3 earthquake that struck in Modena, Italy on the 23rd of May 2012, as recorded by the National Institute of Geophysics and Volcanology (INGV). In Section II, we present the methodology employed for SOP data collection and the concept behind SOP Angular Speed (SOPAS), while Section III describes the case scenario, including additive strain concept. Section IV introduce the ML model's training, validation and testing results. Finally, Section V, concludes the discussion.

II. METHODOLOGY

A long optical fiber cable is, to a good approximation, equivalent to a concatenation of small sections, referred to as plates. Segmenting the fiber into these sections helps define the effect of internal birefringence caused by fiber's construction imperfections on the change in light's SOP. This is because, in a fiber section small enough, the internal birefringence can be considered uniform. Consequently, any deviation observed in SOP, diverging from the anticipated uniform internal behavior effect, indicates an external stressor. This approach is referred to as the Waveplate model [17], depicted in Fig. 2.
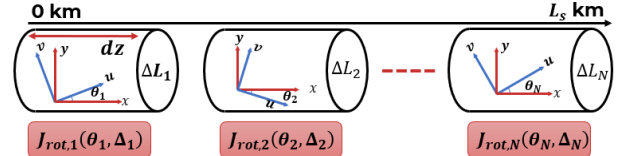

Fig. 2. Waveplate Model Concept

Simulation splits the fiber of L_s km into N waveplates of length dz. Each waveplate is assigned with two random angles: ellipse of polarization or the major axis angle, and the eccentricity of the ellipse. In our modeling, we only consider the major axis angle as it refers to the internal birefringence axes. Each major axis angle is randomly rotated by θ, while the external fiber strain induces a phase shift Δ_i between the orthogonal components:

$$\Delta_i = f(\text{strain}) \tag{1}$$

The Jones output state of polarization $J_{\text{out}}(t)$ is obtained by multiplying the input SOP J_{in} by the sequence of waveplates' Jones rotation matrices.

$$J_{out} = \prod_{k=1}^{N} J_k(\theta_k, \Delta_k) \cdot J_{in} \tag{2}$$

We extend the use of this model to integrate the conventional i-DAS conversion in order to convert earthquake ground displacement values to strain-time matrix, where each 116 nm of displacement is equivalent to 11.6 nanostrain, and multiplying by 1×10^9 to obtain the strain [18]. Additionally, using Frequency Domain Integration (FDI) technique, we convert the strain rate of a car passage to strain. FDI technique consists of dividing the data by $-2j\pi n$ in the frequency domain, where n is the temporal frequency, and then transformed back into the time domain [19].

$$\text{Strain}(t) = \mathcal{F}^{-1} \left\{ \frac{\mathcal{F}\{\text{Strain Rate}(t)\}}{-2j\pi n} \right\} \tag{3}$$

Large set of SOP evolution could be extracted from Waveplate simulations for any induced strain values, as in each simulation the plates are assigned to different set of random angles. This set of SOP evolution should hold an invariant parameter linked to a specific strain. A sample of three SOP evolution induced by a car passage strain shown in Fig. 3.
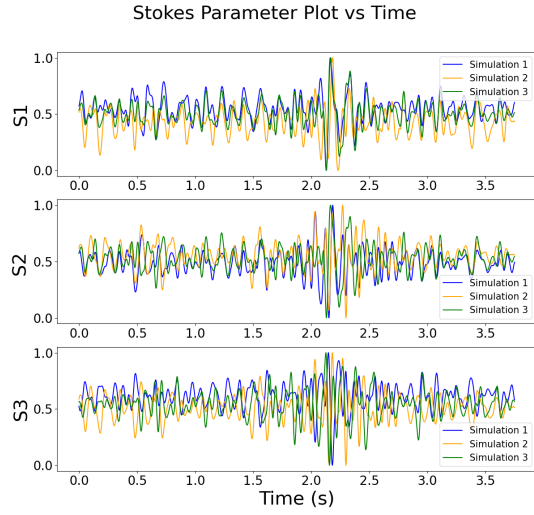
Fig. 3. Three SOP Evolution for Strain Induced by Car Passage - Where in each simulation, random angle is inherently assigned to each plate

To minimize the computational time, and due to the fact that the SOP is represented by the vector k with components $(S1[k], S2[k], S3[k])$, the discrete State of Polarization Angular Speed (SOPAS) denoted by $\omega[k]$ is calculated for each SOP file [20], where $\omega[k]$ is:

$$\omega[k] = \arccos\left(\frac{(\mathbf{S}_k \cdot \mathbf{S}_{k-1})}{\|\mathbf{S}_k\|\|\mathbf{S}_{k-1}\|}\right) \cdot \frac{1}{T_s} \quad (4)$$

and T_s representing the sampling period [20]. Thus, considering one parameter instead of three. This computation is analogous to the discrete-time derivative of an angle. A Monte Carlo analysis is carried out from the resulting SOPAS data to train an ML algorithm capable of detecting primary wave's arrival in a noisy environment and distinguishing between the polarization changes induced by a seismic event and those induced by a car passage.

III. CASE SCENARIO

Like any other stress affecting the fiber buried underground, car vehicles pressing down on the road may affect the physical configuration of the light wave propagating along the cable due to the subsurface deformation induced from the weight applied. This deformation leads to a strain measurable amplitude. When the car is moving, the changes in the strain field as the car passes by are recorded as a strain rate. The deformation at a point in the subsurface is described by Flamant-Boussinesq approximation [21]:

$$u_x(x, y, z) = \frac{F\,x}{4\pi G\,r^2}\left(\frac{z}{r} + \frac{2\nu - 1}{1 + \frac{z}{r}}\right) \quad (5)$$

The particle displacement in the x-direction, denoted as u_x, is defined parallel to the road and the fiber at a point (x, y, z) relative to a point load located at the origin, with y being the distance perpendicular to the road/fiber and z the depth beneath the surface. The distance from the origin is given by

$r = \sqrt{x^2 + y^2 + z^2}$. The point load applies a total force F into an infinite half-space characterized by a uniform shear modulus G and Poisson's ratio ν. The particle velocity $\dot{u}_x$ is obtained by differentiating u_x with respect to time, and noting that $\dot{x}$ is the velocity of the car traveling in the x-direction. There are two types of deformations induced by a car passage, the quasi-static deformation that is controlled by the distance between the fiber and the road, and the dynamic deformation that is determined by the interactions between the car tyres and the road. Dynamic deformation generate surface waves that travel away at seismic speed and are better to be integrated over earthquake strain, as the quasi-static deformation is a very simple impulse response that lack wave propagation information present in the dynamic wave. DAS systems do not measure particle motions, but rather the average longitudinal strain rate between two sensing points. Fig. 4 refers to strain rates induced by a car passage and recorded by DAS in the dynamic frequency band (5-20 Hz) [19]. Exploiting the aforementioned FDI technique, we managed to get the strain values over almost 4 seconds of time period.
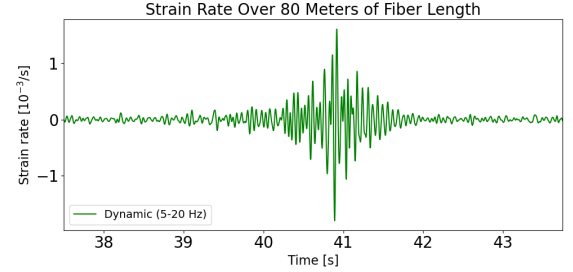

Fig. 4. Strain Rate Induced by a Car Passage - The Strain is induced by the dynamic deformation of the vehicles' weight. Strain rate was recorded by DAS over 80 meters fiber length

We then extracted the samples corresponding to the strain induced by the car passage over a one-second interval, specifically from 40.5 to 41.5 seconds. These samples were then added to the strain values induced by the M4.3 earthquake shown in Fig. 5. Earthquake ground displacement values are
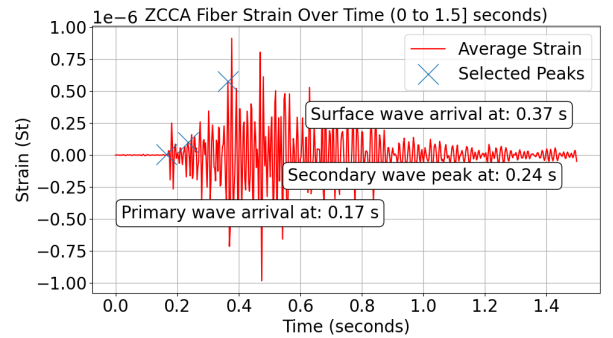

Fig. 5. Strain Induced by Earthquake Ground Displacement Values Recorded by INGV over 80 meters Fiber Length - Slicing time interval 0 to 1.5 out of 0 to 4 seconds for better visualization

recorded by INGV [22] and converted into strain by the

conventional i-DAS conversion employed in our Waveplate model. To add the two strains, fiber cables should have the same characteristics. In previous study [10], we collected data from the ZCCA seismic station located in Zocca municipality in Modena, which is tens of kilometers far from the Modena earthquake epicenter. Then, we integrated the strain induced along a 10 km fiber positioned at the exact geographical coordinates as the station. Since the extracted DAS data from [19] used an 80 meter fiber cable, we selected an equivalent section length from ZCCA fiber. This ensures the same spatial resolution (3.2 meters) and the same sampling rate (400 Hz) are maintained. Selecting a small section of the fiber, compared to the original 10 km length, will affect the time lag between the surface and primary waves arrivals. However, our focus in this paper is not on early warning generation but instead to detect primary wave in a noisy environment and to demonstrate our model's capability to distinguish between various environmental events. For this reason, we started by integrating each of the two strains separately in the Waveplate model in order to visualize a sample of the SOPAS induced by each strain at the output of the fiber as shown in Fig. 6.
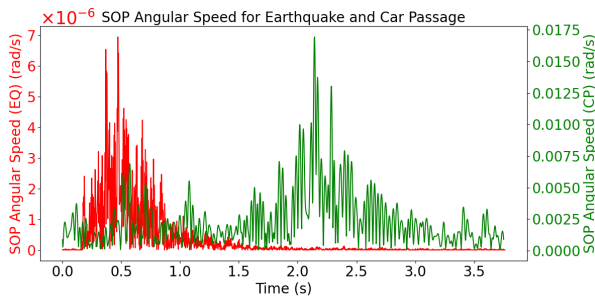

Fig. 6. Red - SOPAS induced by Earthquake Strain; Green - SOPAS induced by Car Passage Strain

Fig. 6 shows an ascending pattern in the red curve (SOPAS induced by the earthquake), and this is because the magnitude increases from the primary wave to the surface wave. The green curve (SOPAS induced by the car passage) shows almost a peak at around 2 seconds, indicating a car passage. To distinguish between the strains and look up for the resulting SOPAS, we add up the one second time window [40.5s - 41.5s], which is equivalent to [1.5s - 2.5s] of the car passage strain, into the earthquake strain starting from 0.2 seconds. Referring to Fig. 5, we have chosen 0.2 seconds to have A = [0.17s - 0.2s], a time interval holding information about primary wave with no car passage and B = [0.2s - 0.24s], a time interval holding noisy information about the primary wave disturbed by a car passage. The one second integrated strain of car passage will end at 1.2 seconds, while the earthquake wave dissipates at almost 1 second. This introduces another class with time interval C = [1s - 1.2s], where only car passage strain is present without any overlapping seismic wave. This additive approach will facilitates the detection of the primary wave in a noisy environment (A), allowing to distinguish between both events (B) and (C). For that

purpose, we ran numerous simulations for the additive strain. An example of SOPAS induced by that strain is shown in Fig. 7. This large set of SOPAS data is divided into portions for training and validation with the remainder used for testing before being utilized in a machine learning model to detect all events.
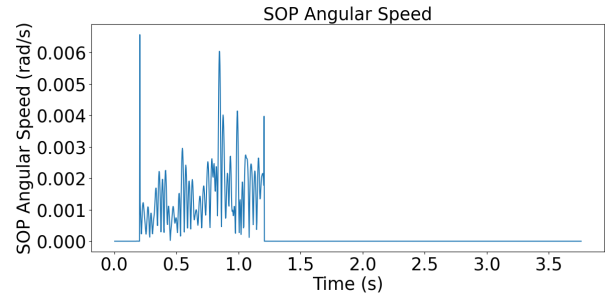

Fig. 7. SOPAS Induced by Additive Strain - Car passage strain over the strain induced by the earthquake

ML MODEL'S VALIDATION AND TESTING RESULTS

The proposed ML model leverages a deep learning architecture designed to capture temporal dependencies and important features within sequential data for a multi-class classification task. The model begins with an input layer to collect sequences of time steps length corresponding to the number of features in input data (SOPAS). To ensure all features are treated equally, we employ the Min-Max Scaler to normalize the input data to a fixed range, typically [0, 1], which stabilizes the training process. This input is analyzed by four Long Short - Term Memory (LSTM) layers [23]. The first LSTM layer consists of 64 units that returns back the full sequence of outputs to allow subsequent layers to further process temporal dependency information. The second LSTM layer increases the units to 128, improving the model's ability to identify complex patterns in the data, while still returning back the full sequence of outputs. The third and fourth LSTM layers consist of 64 units each, utilized for refining the sequence representations. Moreover, the model integrates an attention mechanism [24]. This mechanism begins with a time distributed dense layer with ReLU activation applied at each time step. Attention probabilities are then generated by a softmax activation. These probabilities are used to compute a weighted sum of the LSTM outputs through a dot product operation, highlighting the most informative parts of the sequence. The attention layer refines the model's focus, enhancing performance and interpretability in distinguishing seismic waves. The result is then passed to a fully connected layer of 6 units and softmax activation, which outputs the probability of each class: Primary Wave and Car Passage (P wave-CP), Secondary Wave and Car Passage (S wave-CP), Surface Wave and Car Passage (Surface Wave-CP), Primary Wave and No Car Passage (P wave-NoCP) and No Earthquake but Car Passage (No EQ-CP). Early detection of earthquake in a noisy environment correspond to (P wave-CP), while distinguishing between both events corresponds

to two classes (No EQ-CP to identify car passage event and P wave-NoCP to identify the arrival of earthquake primary wave). The model is compiled with the Adam optimizer and sparse categorical cross-entropy loss. This compilation makes it suitable for integer labeling for the multi-class classification tasks (0 as No Earthquake, 1 as Primary wave, 2 as Secondary Wave, 3 as Surface Wave, 4 as Car Passage and 5 as No Car Passage). Thus, combining two classes of events will hold two integer labels (for example, P wave-CP is equivalent to 14). To enhance generalization and prevent over-fitting, early stopping is implemented to monitor the validation loss and stop training if no improvement is observed over three consecutive epochs, while also to restore the best weights observed during training. This architecture efficiently combines the effectiveness of Long Short - Term Memory networks along with attention mechanisms, make it well-suited for complex sequential data tasks. The model is trained for 100 epochs. Almost 60% of the SOPAS data is used for training, 20% for validation and 20% for testing. Exploiting the Waveplate model, we ran 300 simulations induced by the additive strain, assigning different plates' orientations in each simulation. Fig. 8 shows the model training and validation accuracy.
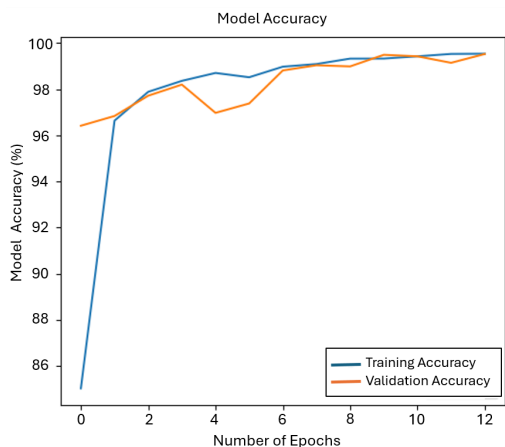

Fig. 8. ML Model Training and Validation Accuracy

Fig. 8 displays the accuracy of the ML model over a sequence of epochs. The model's training accuracy curve shown in blue increases rapidly, indicating effective initial training. The validation accuracy curve shown in orange evaluates the model's ability to predict new unseen data. The proximity of the two curves indicates that the model has been generalized well with a minimal risk of over-fitting. As the number of epochs increases, both curves reach noticeable accuracy rates, implying that additional training is unlikely to yield significant improvements. The model shows a promising level of accuracy for both training and validation datasets, exceeding 95%, with precision, recall, and F1-score all demonstrating similarly high values, indicating strong predictive capability and balance.

As for the model training and validation loss shown in Fig. 9, both curves stabilize near zero, indicating effective learning and minimal over-fitting. Due to the early stopping employed,
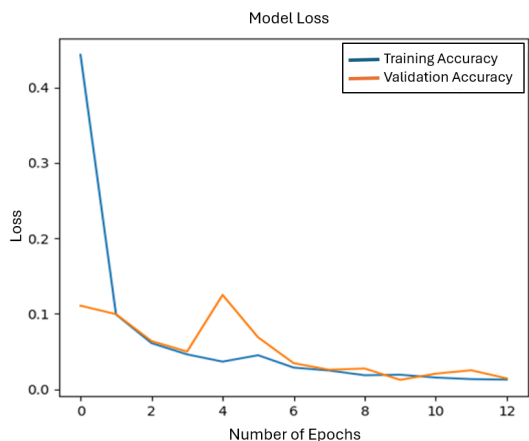

Fig. 9. ML Model Training and Validation Loss

the model stopped at 12 epochs for both model's accuracy and loss. ML testing results for classes' classification is presented by the confusion matrix shown in Fig. 10. The confusion matrix shows the correct and wrong detection by the model. For instance, for P wave-CP class, the model shows 4186 out of 4186 correct detection. For P Wave-NoCP, the model shows 4146 correct detection, 17 wrong detected as Pwave-CP, 4 wrong detected as Surface Wave-CP and 19 wrong detected as No EQ-CP. As for No EQ-CP, 24408 correct detection made by the ML model, 125 wrong detected as P Wave-NoCP, 67 wrong detected as Surface Wave-CP and zeros for other classes. The model shows 99% of accuracy rate in distinguishing between both events (P Wave-NoCP and No EQ-CP) and in detecting the primary wave in a noisy environment (Pwave-CP), giving the opportunity for an early warning before the destructive surface wave strikes.
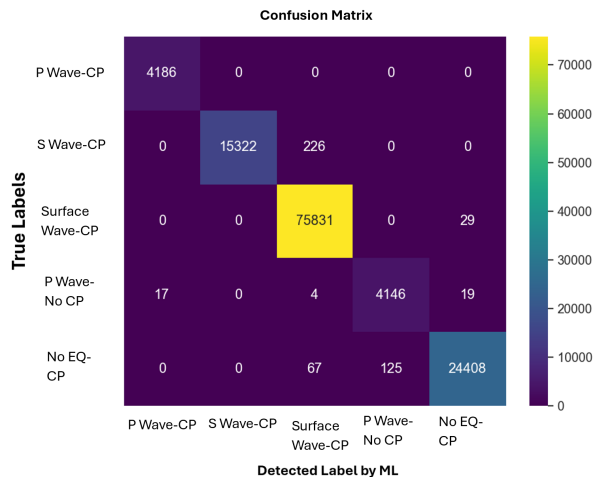

Fig. 10. Confusion Matrix

Furthermore, Fig. 11 shows the performance of our model in detecting all events. The blue lines represent SOPAS data samples generated after incorporating the additive strain of

car passage and seismic activity, while the red dashed lines show the model's detection for all events i.e. P Wave-CP, S wave-CP, Surface Wave-CP, P wave-No CP, and No EQ-CP. The red dashed lines align with the SOPAS data's fluctuations, indicating where the model has identify each class of events. This visual representation is consistent with the findings from the confusion matrix in Fig. 10.
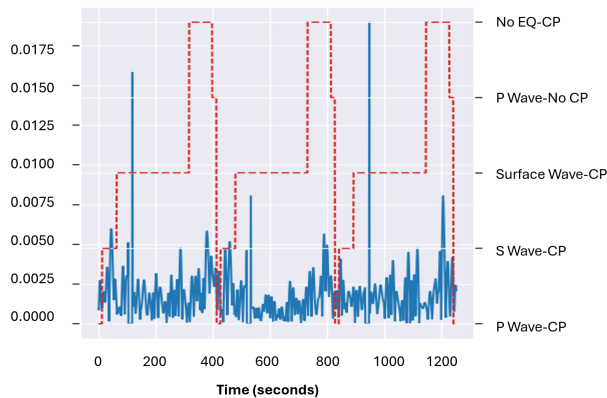

Fig. 11. ML Model's Detection on SOPAS Data Sample

Conclusion

This paper presents an accurate method for early earthquake detection in real-world conditions using a State-of-Polarization sensing mechanism. The promising results of our machine learning approach indicate the potential to exploit the entire existing traffic-carrying optical networks for the simultaneous sensing of various environmental events. This approach represents a cost-effective and efficient solution for early warning systems through early earthquake detection. It enables the implementation of earthquake countermeasures and the rapid initiation of emergency plans. Notably, this technique does not require the addition of dedicated fibers or expensive equipment to the existing network.

Acknowledgment

References

[1] Grand View Research, "Distributed Fiber Optic Sensor Market Size, Share & Trends Analysis Report By Application, By Technology (Rayleigh Effect, Brillouin Scattering), By Vertical (Oil & Gas, Power & Utility), By Region, And Segment Forecasts, 2024 - 2030," 2024. [Online]. Available: https://www.grandviewresearch.com/industry-analysis/distributed-fiber-optic-sensor-sensing-dfos-market. [Accessed: May 27, 2024].

[2] P. Boffi, "Sensing applications in deployed telecommunication fiber infrastructures," in Proceedings of the European Conference on Optical Communication (ECOC), Basel, Switzerland, 2022, pp. 1-4.

[3] X. Zhang, H. Zhu, X. Jiang, and W. Broere, "Distributed fiber optic sensors for tunnel monitoring: A state-of-the-art review," Journal of Rock Mechanics and Geotechnical Engineering, pp. 1-23, 2024.

[4] A. Motil, A. Bergman, and M. Tur, "[INVITED] State of the art of Brillouin fiber-optic distributed sensing," Optics & Laser Technology, vol. 78, pp. 81-103, Part A, 2016.

[5] H.-J. Li, H.-H. Zhu, D.-Y. Tan, B. Shi, and J.-H. Yin, "Detecting pipeline leakage using active distributed temperature sensing: Theoretical modeling and experimental verification, "Tunnelling and Underground Space Technology, vol. 135, no. 105065, 2023.

[6] C. Carver and X. Zhou, "Polarization sensing of network health and seismic activity over a live terrestrial fiber-optic cable," Communications Engineering, vol. 3, pp. 1-12, 2024.

[7] W. Zhu, E. Biondi, J. Li, J. Yin, Z. E. Ross, and Z. Zhan, "Seismic arrival-time picking on distributed acoustic sensing data using semi-supervised learning," Nature Communications, vol. 14, no. 8192, 2023.

[8] J. Yin, M. Soto, J. Ramírez, V. Kamalov, W. Zhu, A. Husker, and Z. Zhan, "Real-data testing of Distributed Acoustic Sensing for offshore earthquake early warning," The Seismic Record, vol. 3, pp. 269–277 2023.

[9] G. Marra, C. Clivati, R. Luckett, et al., "Ultrastable laser interferometry for earthquake detection with terrestrial and submarine cables," Science, vol. 361, pp. 486-490, 2018.

[10] H. Awad, F. Usmani, E. Virgillito, R. Bratovich, R. Proietti, et al. "Environmental surveillance through machine learning-empowered utilization of optical networks," Sensors, vol. 24, pp. 3041, 2024.

[11] E. Virgillito, H. Awad, R. Bratovich, et al., "Earthquake emulation for environmental sensing interrestrial telecom networks," in Proc. Frontiers in Optics + Laser Science (FiO, LS), Tacoma, Washington, United States, 2023, pp. FM1D.4.

[12] F. Usmani, H. Awad, E. Virgillito, et al., "Earthquake early warning through terrestrial optical networks: A Bi-GRU attention model approach on SOP data," in Proc. Optical Fiber Communication Conference (OFC), San Diego, California, United States, 2024, pp. Tu3J.2

[13] E. Virgillito, H. Awad, F. Usmani, et al., "Detection, localization and emulation of environmental activities using SOP monitoring of IMDD optical data channels," in Proc. 23rd International Conference on Transparent Optical Networks (ICTON), Bucharest, Romania, 2023, pp. 1-4.

[14] H. Awad, E. Virgillito, S. Straullu, et al., "Environmental sensing and localization via SOP monitoring of IM-DD optical data channels," in Proc. OPTICA Sensing Congress (OSA), Munich, Germany, 2023, pp. JTu4A.8.

[15] E. Virgillito, S. Straullu, F. Aquilino, et al., "Detection and localization of metropolitan anthropic activities by SOP monitoring of IM-DD optical data channels," in Proc. International Conference on Photonics in Switching and Computing (PSC), Mantova, Italy, 2023, pp. 1-3.

[16] H. Awad, F. Usmani, E. Virgillito, et al., "Seismic detection through state-of-polarization analysis in optical fiber networks," in Proc. SPIE Photonics West, San Francisco, California, United States, 2024, pp. 12835–48.

[17] F. Curti, B. Daino, G. D. Marchis, and F. Matera, "Statistical treatment of the evolution of the principal states of polarization in single-mode fibers," Journal of Lightwave Technology, vol. 8, no. 8, pp. 1162–1166, 1990.

[18] D. Fratta, "Overview and preliminary results from the porotomo project at Brady Hot Springs, Nevada: Poroelastic tomography by adjoint inverse modeling of data from seismology, geodesy, and hydrology," in Proc. 42nd Workshop on Geothermal Reservoir Engineering, Stanford, California, United States, 2017, SGP-TR–212.

[19] M. van den Ende, A. Ferrari, A. Sladen, and C. Richard, "Deep deconvolution for traffic analysis With Distributed Acoustic Sensing data," IEEE Transactions on Intelligent Transportation Systems, vol. 24, no. 3, pp. 2947-2962, 2023.

[20] S. Pellegrini, G. Rizzelli, M. Barla, and R. Gaudino, "Algorithm optimization for rockfalls alarm system based on fiber polarization sensing," IEEE Photonics Journal, vol. 15, no. 7100709, pp. 1–9, 2023.

[21] S. Yuan, A. Lellouch, R. G. Clapp, and B. Biondi, "Near-surface characterization using a roadside distributed acoustic sensing array,"Lead. Edge, vol. 39, no. 9, pp. 646–653, 2020

[22] INGV, "Italian National Institute of Geophysics and Volcanology," 2024. [Online]. Available: http://ismd.mi.ingv.it/ismd.php?tipo=lista. [Accessed: Apr. 20, 2024].

[23] S. Hochreiter and J. Schmidhuber, "Long short-term memory," Neural computation, vol. 9, no. 8, pp. 1735–1780, 1997.

[24] Y. Jia, "Attention mechanism in machine translation," Journal of Physics: Conference Series, vol. 1314, pp. 012186, 2019.